

Supporting Information

For

Heteroatom-Substituted Delaminated Zeolites as Solid Lewis-Acid Catalysts

Xiaoying Ouyang¹, Son-Jong Hwang², Dan Xie³, Thomas Rea³, Stacey I. Zones^{*.1.3}, Alexander Katz^{*.1}

¹Department of Chemical and Biomolecular Engineering, University of California at Berkeley, Berkeley,
California 94720

²Department of Chemical Engineering, California Institute of Technology, Pasadena, California 91125

³ Chevron Energy Technology Company, Richmond, California 94804

* Corresponding Author: sizo@chevron.com, askatz@berkeley.edu

Characterization Methods.

PXRD. Powder X-ray diffraction (PXRD) patterns were collected on a Bruker GADDS D-8 diffractometer using a Cu K α radiation. Data were collected in the 2θ range from 3° to 30° with a step size of 0.02° and a dwell time of 2 s. LeBail-type whole-pattern profile-fitting^{1,2} was performed using the GSAS-EXPGUI software package^{3,4}. The peak shape function used to fit the powder patterns is the modified Thompson-Cox-Hastings pseudo-Voigt function.⁵ Peak asymmetry due to axial divergence was calculated by the model proposed by Finger et al.⁶

Solid-state NMR. Solid-state ^{29}Si NMR spectroscopy experiments were performed at ambient conditions using a Bruker Avance 500 MHz spectrometer with a wide-bore 11.7 T magnet and employing a 4-mm MAS probe (Bruker). The spectral frequencies were 99.4 MHz for the ^{29}Si nuclei. ^{29}Si CPMAS NMR (CP contact time of 2 ms) and ^{29}Si MAS NMR spectra (after a $4\ \mu\text{s}$ - 90° pulse) were acquired with application of a strong ^1H decoupling pulse at 8 kHz of sample spinning. The recycle-delay time for the Bloch decay was 300 s. External references were used to calibrate the NMR chemical shifts, and spectra were reported with reference to tetramethylsilane (TMS) for ^{29}Si nuclei.

PXRD Characterization

PXRD patterns for the as-made precursor ERB-1P, calcined ERB-1C, all-silica delaminated DZ-1, and heteroatom-substituted delaminated DZ-1 materials are shown in Figure S2(a). The powder patterns of ERB-1P, ERB-1C, DZ-1, and Ti-DZ-1 are indexed on the basis of primitive hexagonal unit cells, as shown in Figure S2(b). Low-angle peaks at 3.19° (reflection (001)) and 6.55° (reflection (002)) represent the layered structure of ERB-1P. Peaks at 7.16°

(reflection (100)), and 7.95° (reflection (101)) in pattern (i) in Figure S2(b) are consistent with previously published data for ERB-1P.⁷ Similar to previous observations by Millini et al., the intensities corresponding to *c*-axis features (i.e. (001) and (002) reflections) decrease significantly after ERB-1P calcination at 550°C in pattern (ii) in Figure S2(a) and S2(b). This has been previously attributed to the formation of 10-MR structures between layers, which cause a loss of long-range order along the *c*-axis.⁸ The (002) reflection shifted from 6.55° in ERB-1P to a value of about 6.97° for ERB-1C, and merged with the (100) reflection at 7.08° , which makes a slightly split peak at around 7.04° for ERB-1C in pattern (ii) in Figure S2(a). Such a shift in the (002) reflection corresponds to a significant contraction of the unit cell, from 26.99 \AA in ERB-1P to 24.76 \AA in ERB-1C along the *c*-axis, as shown in Table 1. A contraction along the *a*-axis from 14.29 \AA in ERB-1P to 14.06 \AA in ERB-1C is also observed. Both of these contractions are accompanied by loss of the organic template (PI) during calcination.

Delamination of ERB-1P causes a loss of long-range order along the *c*-axis and pronounced structural changes in the *a-b* plane. This is shown by a comparison of pattern (iii) in Figure S2(b) for DZ-1 with that of the calcined material ERB-1C. As in ERB-1C, the (001) reflection for DZ-1 is too weak to be identified. The (002) reflection is 6.97° in ERB-1C and is 7.20° in DZ-1 in Figure S2(b). The (100) reflection for DZ-1 also exhibits a small but significant shift to lower 2θ angles relative to that for ERB-1C in Figure S2(b). The PXRD data of ERB-1P, ERB-1C, DZ-1, and Ti-DZ-1 were analyzed using whole-pattern profile-fitting^{1,2} for $2\theta = 3 - 30^\circ$. As shown in Table S1, this fitting demonstrates a contraction of the unit cell along the *c*-axis, from 24.76 \AA to 23.76 \AA , and a unit cell expansion of 0.06 \AA along the *a*-axis accompanying delamination, when comparing DZ-1 and ERB-1C. The latter expansion is likely caused by the formation of silanol nests which after delamination contain hydrogen bonds at the T-positions

where previously, prior to delamination, B atoms were condensed. The PXRD pattern and unit-cell parameters for Ti-DZ-1 are quite similar to DZ-1, probably due to the low Ti concentration in the material ($\text{Si/Ti} = 67$ for Ti-DZ-1).

The sharp peaks for the (101) and (102) reflections in both ERB-1P and ERB-1C are no longer observed in both DZ-1 and Ti-DZ-1, as shown in patterns (iii) and (iv) in Figure S2(b). Instead, a broad band between 8° and 11° due to overlapping (101) and (102) reflections is clearly observed, and the relative intensity of this broad band has been previously used as a metric for evaluating the extent of delamination.⁹ In patterns (iii, iv) in Figure S2(b), the (101) and (102) reflections for DZ-1 are much lower in intensity compared with patterns (i) and (ii) for ERB-1P and ERB-1C, respectively, in Figure S2(b). This is consistent with a lack of layer alignment in DZ-1, when using our synthetic delamination approach relying on $\text{Zn}(\text{NO}_3)_2$ treatment.

Heteroatom-substituted DZ-1 materials have very similar PXRD patterns as previously reported Ti-DZ-1, as shown in Figure S2(a), which suggests that incorporation of heteroatom metals in part of the silanol nests located within 12-MR near the external surface does not alter the long-range order of the material, and the high surface area and disordered arrangement along *c*-axis are still preserved.

Solid-State NMR Spectroscopy

²⁹Si MAS and CPMAS NMR spectra shown in Figure S2 characterize the local structure of Si in ERB-1C, DZ-1, Sn-DZ-1, and Ti-DZ-1. All spectra in Figure S2 show the absence of a Q^2 ($\equiv(\text{SiO})_2\text{Si}(\text{OH})_2$) resonance, which would otherwise be expected to appear at approximately -

80 ppm to -90 ppm.¹⁰ This is strong corroborating evidence that there is no amorphization of the zeolite framework accompanying delamination during our treatment procedure. A comparison of the ²⁹Si MAS and ²⁹Si CPMAS spectra for each sample demonstrates the presence of silanol-related resonances (i.e. the -101 ppm resonance representing Q³ ($\equiv(\text{SiO})_3\text{SiOH}$) Si atoms is stronger than resonances centered around -105 ppm representing Q⁴ ($\equiv(\text{SiO})_4\text{Si}$) Si atoms in the CPMAS spectrum, which is opposite to the observed relative intensity trend in the MAS spectrum). The specific assignments of Q³ and Q⁴ resonances are consistent with results previously reported by Cambor et al. for ITQ-1 material^{11,12} and is as follows: -94.8 ppm (Q³), -100.9 ppm (Q³), -105.2 ppm (Q⁴), -110.3 ppm (Q⁴), -113.1 ppm (Q⁴), -116.5 ppm (Q⁴), and -119.5 ppm (Q⁴). Previously, we demonstrated that delamination results in significantly sharper Q³ resonances (-101 ppm) in the ²⁹Si CPMAS NMR spectra of Al-exchanged delaminated ERB-1 materials, relative to 3D zeolite ERB-1C, as a result of fewer 10-MR formed via condensation between layers.⁷ For the delaminated materials synthesized via the Zn(NO₃)₂ route, besides the Q³ resonance (-101 ppm) due to uncondensed hydroxyl groups between layers, we also expect another Q³ resonance due to hydroxyl groups associated with the silanol nests, which are formed during delamination with Zn(NO₃)₂ when framework B is removed. Indeed, the ²⁹Si CPMAS NMR spectra of DZ-1 (Figure S2(b)) shows a very sharp resonance at -98 ppm, which is assigned to hydroxyls of silanol nests, as well as a shoulder at -101 ppm¹³ for the uncondensed hydroxyl groups. Both Q³ resonances (-98 ppm and -101 ppm) are not observed on the ²⁹Si CPMAS NMR spectra of 3D zeolite ERB-1C (Figure S2(a)). This assignment is partially based on precedent from Wu et al., who observed similar Q³ resonances for hydroxyl groups associated with silanol nests in the zeolite mordenite (MOR).¹⁴

Sn-DZ-1 and Ti-DZ-1 were synthesized from DZ-1 by reoccupying some of the silanol nests with tetrahedral Sn and Ti sites, respectively. Such substitution of Sn and Ti should be accompanied by a general reduction in the number density of hydroxyl groups which are associated with silanol nests. Therefore, based upon our assignment above, we expect to see lower intensity in the Q^3 resonances in ^{29}Si CPMAS NMR spectra at -98 ppm for Sn-DZ-1 and Ti-DZ-1, respectively. From Figure S2(c) and S2(d), we clearly observe weaker-intensity Q^3 resonances in the ^{29}Si CPMAS NMR spectrum of Sn-DZ-1 and Ti-DZ-1 relative to DZ-1 (see Figure S2(b)), which suggests that the heteroatoms Sn and Ti have been successfully incorporated in some of the accessible near-surface silanol nests as these sites become repopulated again with framework T-atoms. The general reduction in the Q^3 resonance assigned at -98 ppm for heteroatom-substituted DZ-1 samples above, together with results from DR-UV spectroscopy in Figure 5, strongly suggest that the heteroatoms are located in isolated framework T-positions. However, as previously suggested for hydrated Al cations,^{15,16} due to the bulky size of the heteroatom precursors (i.e. SnCl_4 and $\text{Ti}(\text{OC}_4\text{H}_9)_4$), the heteroatoms are able to access only near-surface silanol nests, and are not able to enter the 10-MR channels and repopulate those located internally. Another interesting observation is that, Ti-DZ-1 with $\text{Si}/\text{Ti} = 67$ (see Supporting Information Figure S2(d)) seems to have relatively lower intensity in its Q^3 resonance at -98 ppm in the ^{29}Si CPMAS NMR spectra than does Sn-DZ-1 with $\text{Si}/\text{Sn} = 75$ (see Supporting Information Figure S2(c)). This can be rationalized on the basis of slightly higher heteroatom content (and lower subsequent hydroxyl content) in Ti-DZ-1 ($\text{Si}/\text{Ti} = 67$) compared with Sn-DZ-1 ($\text{Si}/\text{Sn} = 75$).

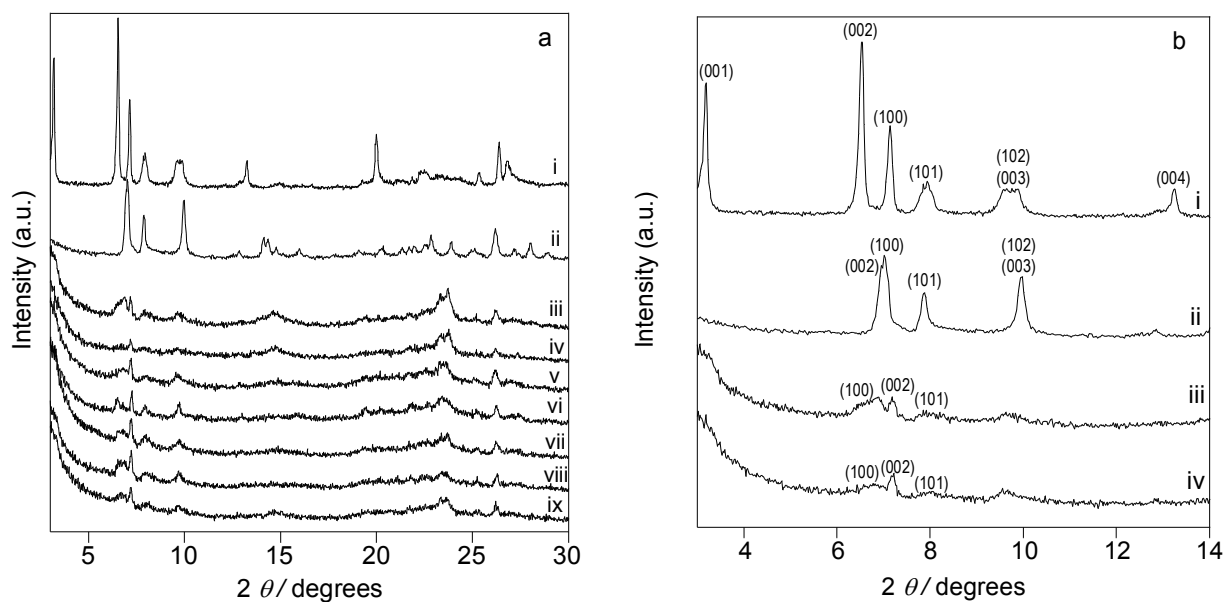


Figure S1. (a) Indexed PXRD patterns in $2\theta = 3\text{--}14^\circ$ exhibiting reflection positions, as obtained from whole-pattern profile-fitting, for materials (i) ERB-1P, (ii) ERB-1C, and (iii) DZ-1. (b) PXRD patterns in $2\theta = 3\text{--}30^\circ$ characterizing (i) ERB-1P, (ii) ERB-1C, (iii) DZ-1, (iv) Sn-DZ-1, (v) Ti-DZ-1, (vi) Zr-DZ-1, (vii) Hf-DZ-1, (viii) Nb-DZ-1, and (iv) Ta-DZ-1.

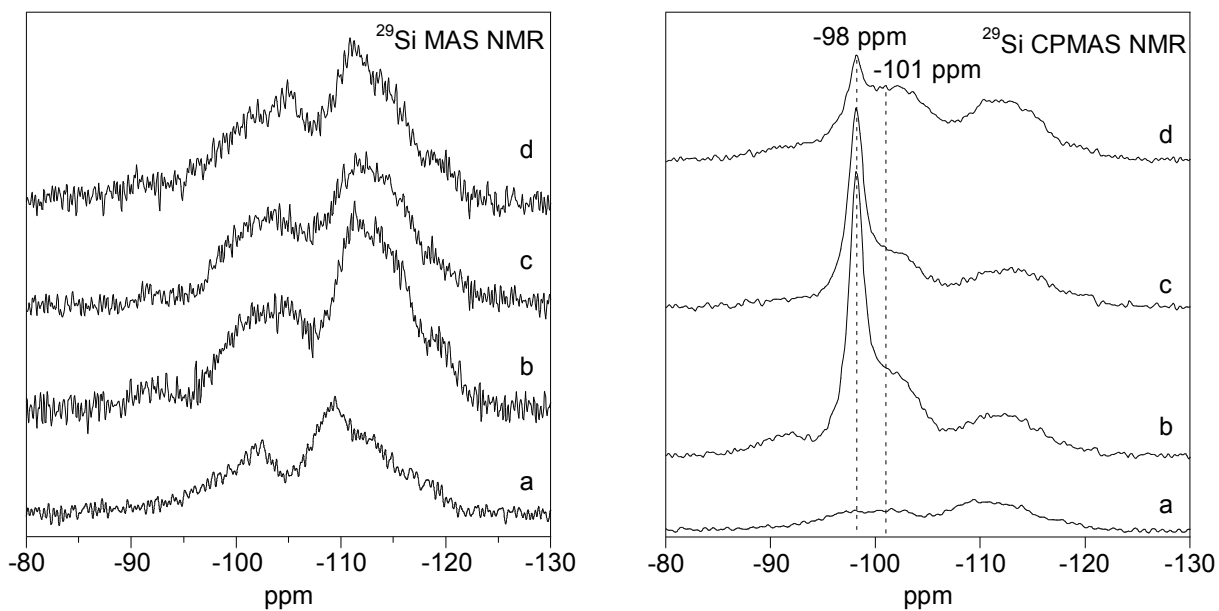


Figure S2. ^{29}Si MAS and ^{29}Si CPMAS NMR data characterizing (a) ERB-1C (Si/B = 10), (b) DZ-1, (c) Sn-DZ-1 (Si/Sn = 75), and (d) Ti-DZ-1 (Si/Ti = 67).

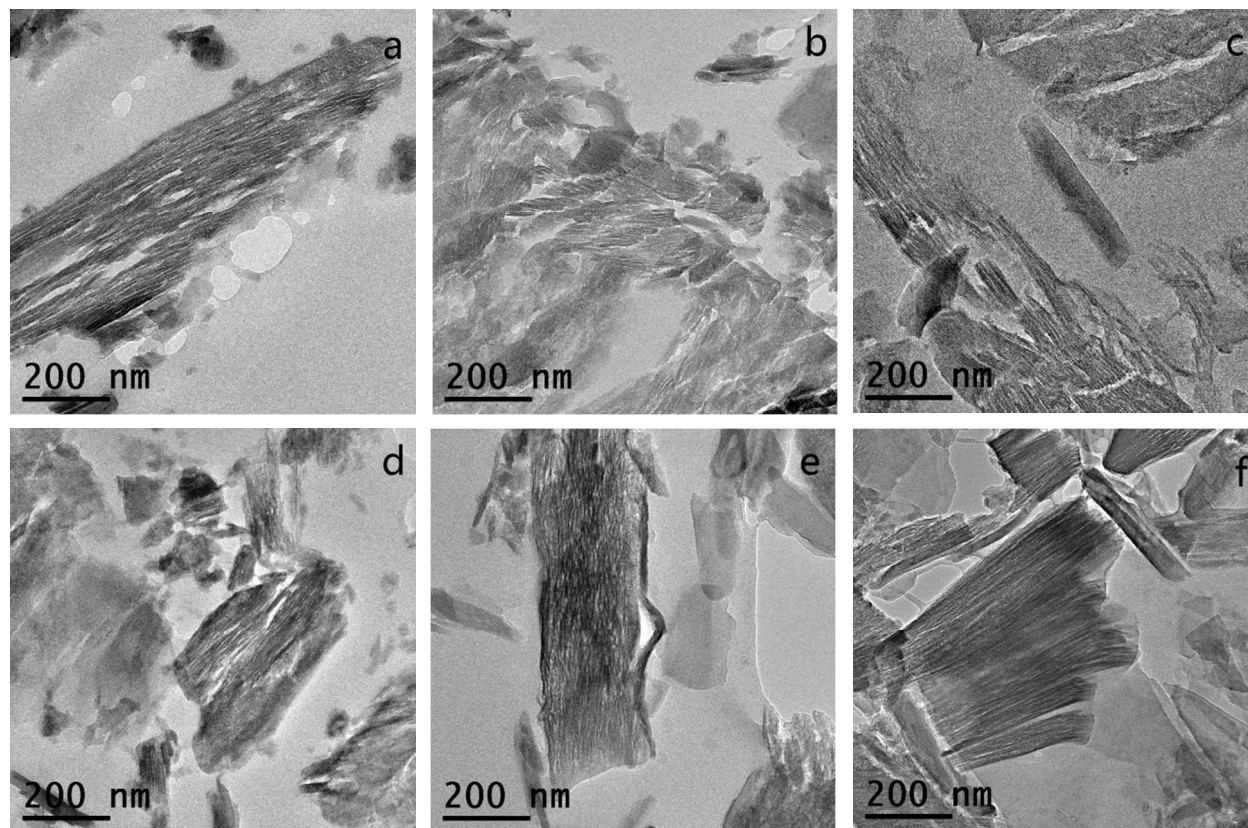


Figure S3. TEM images characterizing (a, b) DZ-1, (c, d) Sn-DZ-1, and (e, f) Ti-DZ-1.

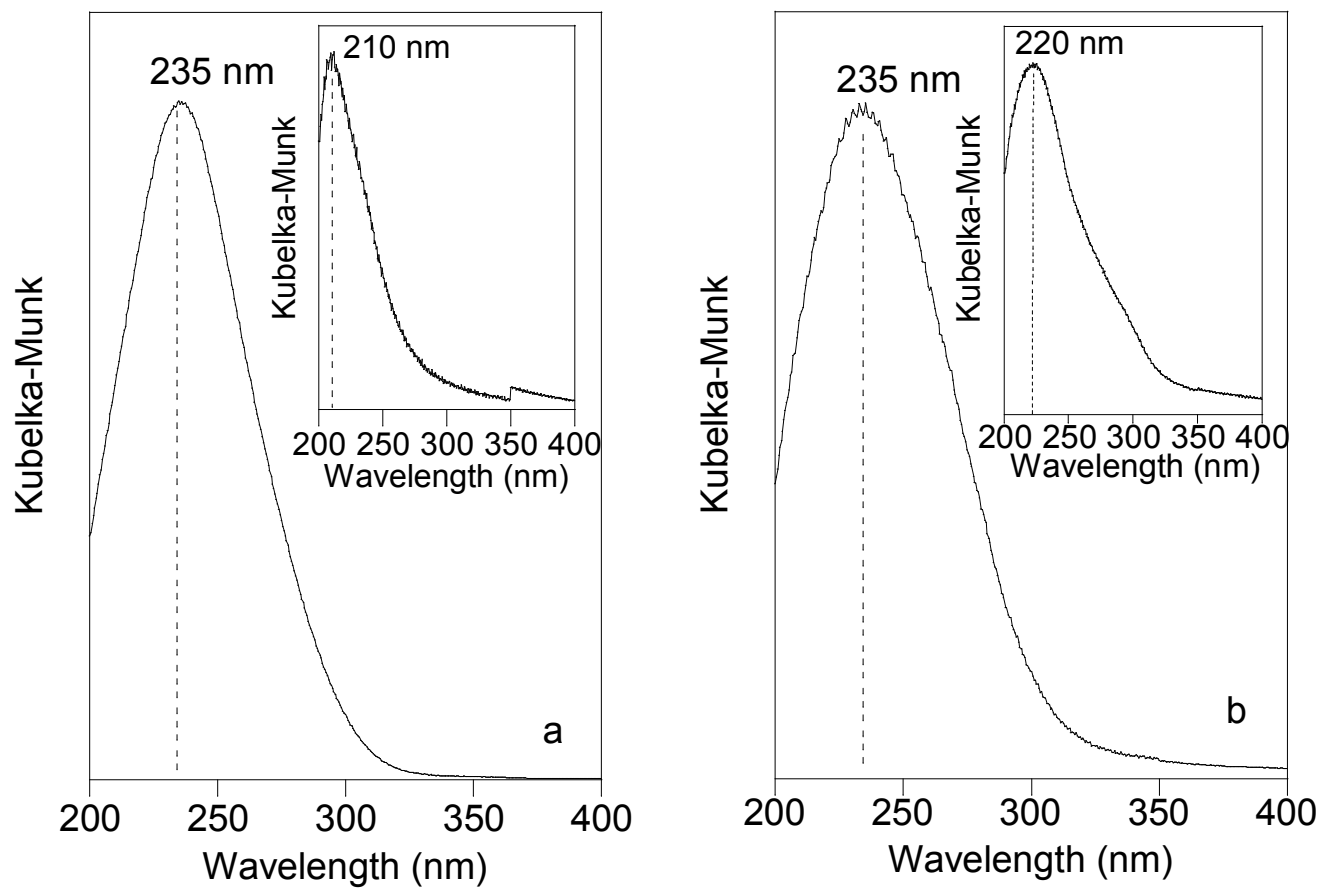


Figure S4. DR-UV data characterizing (a) Ti-DZ-1 and (b) Ti-UCB-4. The inset shows the DR-UV data characterizing the samples after acid treatment.

Table S1. Unit cell parameters of as-made, calcined, and delaminated ERB-1 materials

Sample	Treatment	a (Å)	c (Å)
ERB-1P	As-made and air-dried	14.29	26.99
ERB-1C	Directly calcined at 550 °C	14.06	24.76
DZ-1	Delaminated in Zn(NO ₃) ₂ solution (pH = ~1) at 135 °C	14.11	23.76
Ti-DZ-1	Ti re-inserted DZ-1	14.11	23.76
Sn-DZ-1	Sn re-inserted DZ-1	14.10	23.74

References

- (1) Le Bail, A.; Duroy, H.; Fourquet, J. L. *Mater. Res. Bull.* **1988**, *23*, 447-452.
- (2) Le Bail, A. *Powder Diffr.* **2005**, *20*, 316-326.
- (3) Larson, A. C.; Von Dreele, R. B. *Los Alamos National Laboratory Report LAUR* **2000**, 86-748.
- (4) Toby, B. H. *J. Appl. Cryst.* **2001**, *34*, 210-213.
- (5) Thompson, P.; Cox, D. E.; Hastings, J. B. *J. Appl. Cryst.* **1987**, *20*, 79-83.
- (6) Finger, L. W.; Cox, D. E.; Jephcoat, A. P. *J. Appl. Cryst.* **1994**, *27*, 892-900.
- (7) Ouyang, X.; Hwang, S.-J.; Runnebaum, R. C.; Xie, D.; Wanglee, Y.-J.; Rea, T.; Zones, S. I.; Katz, A. *J. Am. Chem. Soc.* **2013**, *136*, 1449-1461.
- (8) Millini, R.; Perego, G.; Parker, W. O.; Bellussi, G.; Carluccio, L. *Microporous Mater.* **1995**, *4*, 221-230.
- (9) Roth, W. J.; Dorset, D. L. *Microporous Mesoporous Mater.* **2011**, *142*, 32-36.
- (10) Lippmaa, E.; Maegi, M.; Samoson, A.; Engelhardt, G.; Grimmer, A. R. *J. Am. Chem. Soc.* **1980**, *102*, 4889-4893.
- (11) Cambor, M. A.; Corell, C.; Corma, A.; Díaz-Cabañas, M. J.; Nicolopoulos, S.; González-Calbet, J. M.; Vallet-Regí, M. *Chem. Mater.* **1996**, *8*, 2415-2417.
- (12) Cambor, M. A.; Corma, A.; Díaz-Cabañas, M. J.; Baerlocher, C. *J. Phys. Chem. B* **1998**, *102*, 44-51.
- (13) Ouyang, X.; Wanglee, Y.-J.; Hwang, S.-J.; Xie, D.; Rea, T.; Zones, S. I.; Katz, A. *Dalton Trans.* **2014**, *43*, 10417-10429.
- (14) Wu, P.; Komatsu, T.; Yashima, T. *J. Phys. Chem.* **1995**, *99*, 10923-10931.
- (15) Chen, C. Y.; Zones, S. I. In *13th International Zeolite Conference*; Galarneau, A., Di Renzo, F., Fujula, F., Vadrine, J., Eds.; Elsevier: Amsterdam, 2001, p 26-O-05.
- (16) Chen, C. Y.; Zones, S. I. In *13th International Zeolite Conference*; Galarneau, A., Di Renzo, F., Fujula, F., Vadrine, J., Eds.; Elsevier: Amsterdam, 2001, p 11-P-16.